Rayleigh-Bénard percolation transition of thermal convection in porous media: Computational fluid dynamics, NMR velocity mapping, NMR temperature mapping

Markus Weber and Rainer Kimmich
Sektion Kernresonanzspektroskopie, Universität Ulm, 89069 Ulm, Germany
(Received 17 June 2002; published 6 November 2002)

Stationary thermal convection and heat conduction were studied in random-site percolation clusters in a Rayleigh-Bénard configuration experimentally by NMR microscopy techniques and numerically with the aid of a finite volume method. The porosity of the percolation clusters, and the temperature difference applied to the convection cell were varied. Two-dimensional percolation networks were generated with the aid of a random-number algorithm. The resulting clusters were used as templates for the fabrication of model objects. The convective velocity distribution of silicon oil or ethylene glycol filled into the pore space was mapped and evaluated in the form of histograms. The flow patterns visualized in the simulated and the measured velocity maps show good coincidence. In the histograms, two velocity regimes can be distinguished and attributed to local convection rolls responsible for the low-velocity part, and cluster-spanning flow loops characterized by a high-velocity cut-off, respectively. The maximum velocity as a function of the porosity and the overall temperature difference is shown to be indicative for the hydro-thermodynamic Rayleigh-Bénard instability and the geometrical percolation threshold. The coincidence of the Rayleigh-Bénard instability (modified for porous media) and the percolation transition (modified for closed loops) gives rise to a new critical phenomenon termed the Rayleigh-Bénard percolation transition. It occurs at a certain combination of the porosity and the overall temperature difference in the cell. Temperature maps were recorded with the aid of a relaxation-based NMR technique. The consequence of different thermal conductivities in the matrix and in the fluid is that horizontal-temperature gradients arise even in the absence of flow. This leads to a superposition of uncritical convective flow driven by the horizontal-temperature gradients whenever closed-loop pathways are possible and the critical Rayleigh-Bénard convection based on vertical-temperature gradients.

DOI: 10.1103/PhysRevE.66.056301 PACS number(s): 44.30.+v, 47.55.Mh, 44.25.+f, 76.60.Pc

I. INTRODUCTION

This study refers to a combination of two critical phenomena: The percolation transition occurring in random pore networks in the form of a ''geometrical phase transition'' at a certain threshold value p_c of the porosity of the system [1]. The Rayleigh-Bénard transition on the other hand is known for thermal convection in a bulk fluid confined in a cell with variable vertical-temperature gradient [2–4].

Each of the two transition phenomena obviously has its own specific impact on fluid transport. Convective flow anticipates percolation clusters permitting closed-loop transport. It is not just the linear extension of the percolation clusters that determines the largest convection roll. If the pore space network does not allow for closed-loop transport, thermal convection cannot arise.

The classical Rayleigh-Bénard problem refers to bulk fluids confined between a hot bottom and a cold top cover of a cell of ''infinite'' width. The onset of convection at a certain instability condition, the critical Rayleigh number [4], indicates that the hot-fluid buoyancy overwhelms the effect of gravity so that heat conduction becomes surpassed by coherent flow in the form of rolls. In a porous medium the situation is more complex. The thermal conductivities in the fluid and in the solid matrix are normally different. That is, the temperature gradient effective for Rayleigh-Bénard convection depends on the matrix structure and must be examined separately. A further consequence of the complex distribution of thermal conductivities is also that finite horizontal-temperature gradient components arise even in the absence of convective flow. That is, ''uncritical,'' horizontal-gradient based convection occurs whenever a closed-loop pathway of the porous matrix permits continuous flow.

The vertical-temperature gradient component may also cause convection which then is expected to be subject to the familiar bouyancy/gravity interplay of the Rayleigh-Bénard problem. This suggests a thermo and hydrodynamic instability at certain values of a sort of Rayleigh number suitably modified for porous media. That is, convective flow due to the relatively weak horizontal temperature gradient is superimposed by the critical onset of convection rolls induced by vertical-temperature gradients.

The coincidence of the hydro-thermodynamic Rayleigh-Bénard instability (modified for porous media) and the geometrical percolation threshold (modified for closed-loop transport ways) for fluids in porous media forms a new transition phenomenon combining the critical features of both transitions at a time. It is termed ''Rayleigh-Bénard-percolation transition'' and was first described in our previous paper [5]. The crucial experimental parameters are the porosity of the matrix and the vertical-temperature gradient component effective on the length scale of the convection loops. As will be demonstrated in this paper, this combined double-critical phenomenon can only occur at a special combination of these parameters, so that the criticality of both basic effects is accounted for. Experimental parameters other than the porosity and the overall bottom-top temperature difference are the viscosity and thermal conductivity characteristics of the fluid.

In our previous paper [5] it was shown that such critical convection effects can be monitored by relating the maximum coherent-flow velocity in the system with the parameters mentioned and the system size. Coherent flow was examined with the aid of computational fluid dynamics and, as far as resolvable, by nuclear magnetic resonance (NMR) velocity mapping. The objective of the present study is to elaborate the conditions and the features of the Rayleigh-Bénard-percolation transition in random-site percolation clusters in more detail. Furthermore a special NMR technique is reported permitting us to map the temperature in the sample experimentally (in comparison to numerical solutions). This is of crucial importance for the elucidation of the thermodynamic part of the phenomenon.

II. PERCOLATION MODEL OBJECTS AND THE RAYLEIGH-BÉNARD CELL

Two-dimensional random-site percolation networks were generated on a square base lattice with the aid of a random-number algorithm. The occupation probability of the base lattice points is identical to the porosity p of the model objects to be fabricated on the basis of the computer-generated networks. The porosity is defined by $p=V_p/V$, where V_p is the volume of the pore space and V being the total volume of the object. All specifications of the percolation networks refer to this definition even when isolated clusters were omitted in the fabrication process because of their inaccessibility from the outside. Infinite-random-site networks are known to have a percolation threshold of $p_c \approx 0.59$ [1,6], a value that is increased somewhat due to the finite size in the present case.

Using the computer-generated networks as templates, quasi-two-dimensional model objects were milled in 3-mm-thick polystyrene plates with the aid of a circuit board plotter [7,8]. The spatial resolution of the fabrication process was 400 μm, so that all details of the liquid-filled pore space can readily be probed experimentally with the spatial resolution of magnetic resonance microscopy [9]. A photo of a typical example is shown in Fig. 1(b) in comparison to the computer-generated template Fig. 1(a). The size of the objects actually referred to in this report was 4 cm in horizontal direction times 2 cm vertically in the network plane corresponding to 100×50 points of the base lattice.

The pore space was filled with silicon oil KT5 (Bayer AG) (thermal conductivity $\lambda_{KT5}=0.133$ W/mK) or ethylene glycol (thermal conductivity $\lambda_{EG}=0.25$ W/mK). The thermal conductivity of the solid polystyrene matrix is $\lambda_{PS}=0.15$ W/mK. Silicon oil is particularly suited for free-convection experiments because of its relatively large thermal volume expansion coefficient of 1.08×10^{-3} 1/K. From the more practical point of view, silicon oil has the advantage of a low gas solubility, so that gas bubbles in the pore space could safely be avoided in contrast to water, for instance.

The thickness of the model objects was chosen thin enough to avoid perceptible transport in the third space dimension so that ''two-dimensional'' behavior was ensured. The velocities evaluated in the third dimension perpendicular to the network plane did not exceed the noise level (≈ 0.04 mm/s). In order to improve the signal-to-noise ratio,

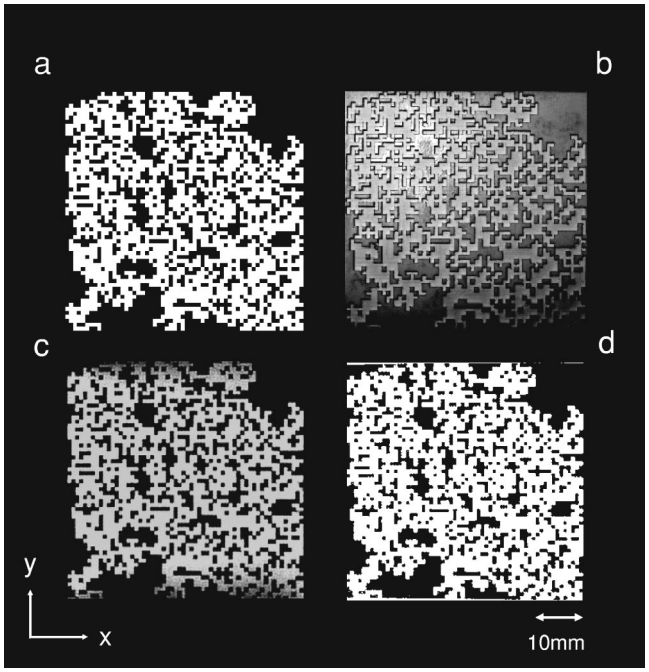

FIG. 1. Percolation network of the type investigated in this study. (a) Computer-generated template for the fabrication of a model object and for computational fluid dynamics. (b) Photograph of the model object. (c) Spin density map of the silicon oil filled pore space. Signals from the solid polystyrene matrix are not rendered with the imaging technique used. (d) Binary representation of the spin density map. This is used as a mask to screen off all matrix pixels in velocity maps in order to avoid undesired velocity noise. The actual object size to which the investigations in this study refer was 4 cm in horizontal direction times 2 cm vertically in the network plane corresponding to 100×50 points of the base lattice.

ten to thirteen identical, 2-mm-deep isolated slices milled according to the percolation template were glued one on top of the other to form a stack of identical percolation networks with a total fluid layer width of 2.6 cm.

The model objects were incorporated in a glass container designed in Rayleigh-Bénard configuration (see Fig. 2). The cooling and heating medium circulating in the top and bottom compartments, respectively, was water. The temperature difference achievable at maximum this way was 70 K, but was restricted to 45 K (silicon oil) and 60 K (ethylene gly-

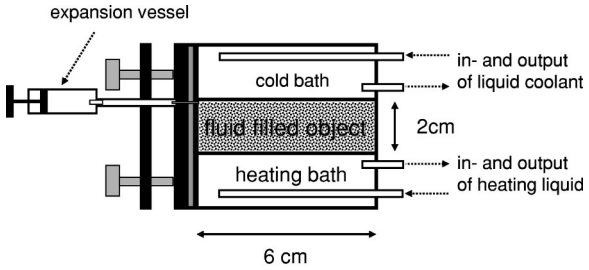

FIG. 2. Schematic representation of the Rayleigh-Bénard convection cell. The model objects were inserted in the middle compartment of size 6 cm$\times$6 cm$\times$2 cm. The top and bottom compartments were cooled and heated with flowing cold and hot water, respectively.

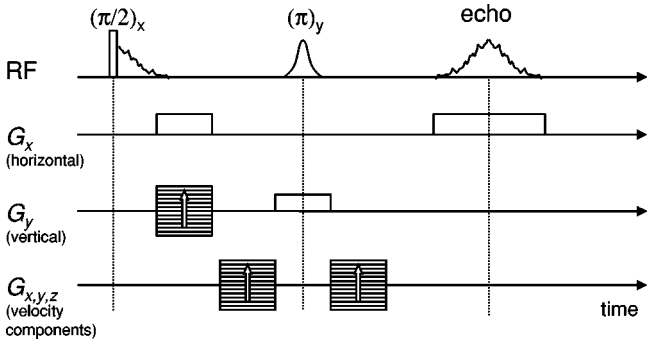

FIG. 3. RF and magnetic flux density gradient (G_x, G_y, G_z) pulse sequence for spin density and velocity mapping. The method employs a Hahn spin-echo RF pulse sequence, a slice selection gradient in the *x* direction (horizontal and perpendicular to the main field flux density), a spatial phase encoding gradient in the *y* direction (vertical and perpendicular to the main field flux density), a spatial frequency encoding gradient in the *z* direction (horizontal and parallel to the main field flux density), and a velocity phase encoding gradient pulse pair directed in different space directions in subsequent experiments depending on the velocity component to be probed. The pulse sequence selectively produces signals from the liquid sample constituents only.

col) in the experiments in order to diminish the danger of breakage of the glass.

III. NMR MICROSCOPY METHODS

A. Spin density and velocity mapping

In the fluid filled space of the model objects NMR velocity mapping experiments were carried out. While thermal convection in free liquids was already studied by different NMR velocity and displacement measuring techniques [10,11], there are only a few literature reports on the application of this technique to porous media [12,13]. It should be mentioned that free-convection patterns in porous media are less susceptible to external distortions and imperfections than in bulk. It is therefore unproblematic to produce stable and reproducible convective flow under such conditions.

The measuring method of the present study was four-dimensional ''Fourier encoding velocity imaging'' probing two spatial and two velocity dimensions. Detailed descriptions of the technique can be found in Refs. [9,14], for instance. Figure 3 shows a scheme of the radio frequency (RF) and magnetic flux density gradient pulses suitable for spin density as well as velocity mapping.

The percolation model object was placed in a Bruker biospec horizontal bore microimaging magnet with a magnetic flux density of 4.7 T corresponding to 200-MHz proton resonance frequency. The RF transmitter and receiver console was home made. Due to strong dipolar line broadening there was no perceptible contribution of the solid polystyrene matrix to the Hahn spin echo signals acquired in our experiments as demonstrated by the spin density map in Fig. 1(c). The velocity maps thus refer exclusively to the fluid in the pore space.

The maps were recorded using the exorcycle of pulse phases [15] in order to remove systematic errors due to imperfections of the pulse sequence. Spatial phase encoding in the vertical *y* direction was incremented typically in 128 steps. The spatial frequency encoding in the horizontal *z* direction was probed by acquisition of typically 256 data points. Slice selection along the *y* direction ensured that the echo signals were restricted to the proper sample and that signals from the heating and cold bath fluids were suppressed. Phase encoding of the velocity was performed for all three space directions in typically seven increments. The raw data sets for each of the velocity components were zero-filled prior to Fourier transformation and were convoluted with a Hanning filter in the direction of the velocity component [16]. The field of view of the spatial dimensions was typically 6 cm (*x* direction) times 3 cm (*y* direction) with a digital resolution between 120 and 240 μm. The velocity range probed was between ± 0.7 and ± 1.3 mm/s with a digital resolution between 0.01 and 0.02 mm/s. Typical spin echo and repetition times were $T_E = 130$ ms and $T_R = 800$ ms, respectively.

The multidimensional Fourier transform of the velocity and space encoded echo signals yields the velocity distribution for each voxel [9]. Velocity maps were rendered by plotting the voxel mean value in the form of gray or color coded contours. Figure 4 shows typical maps of the velocity components v_x (horizontal), v_y (vertical), and of the velocity magnitude, $v = \sqrt{v_x^2 + v_y^2}$ recorded in silicon oil and rendered in this way.

In order to avoid any velocity noise contributions from pixels in the solid matrix, these areas were screened off with the aid of a binary mask obtained from spin density maps (see Fig. 1(d) for example). The mask data set allocates all matrix pixels the value 0 and all pore space pixels the value 1. Figure 1(c) shows a typical spin density map recorded with the aid of the spatial encoding part of the pulse scheme shown in Fig. 3.

B. Temperature mapping

Thermal convection is driven by temperature gradients originating from external heating and cold baths. The spatial distribution of the temperature inside the porous medium is the result of heat conduction and convective flow. Heat conduction is heterogeneous in general because of the different heat conductivities in the pore space fluid and in the solid matrix. It is therefore of interest to measure the local temperature and render it in the form of temperature maps.

Numerous attempts to exploit temperature dependent NMR parameters for indirect temperature measurements in general have been reported in the literature [17–21]. In the present study we decided to use the temperature dependence of the spin-lattice relaxation time T_1 for this purpose. This quantity can readily be mapped by varying the repetition time T_R in a series of experiments with the pulse scheme shown in Fig. 3. The spin-echo amplitude, $E(T_R)$, is then attenuated by partial saturation of the spin state populations according to

$$E(T_R) \propto 1 - c \exp\{-T_R/T_1\}. \tag{1}$$

$c \approx 1$ is a constant.

Since the temperature dependence of T_1 in silicon oil is

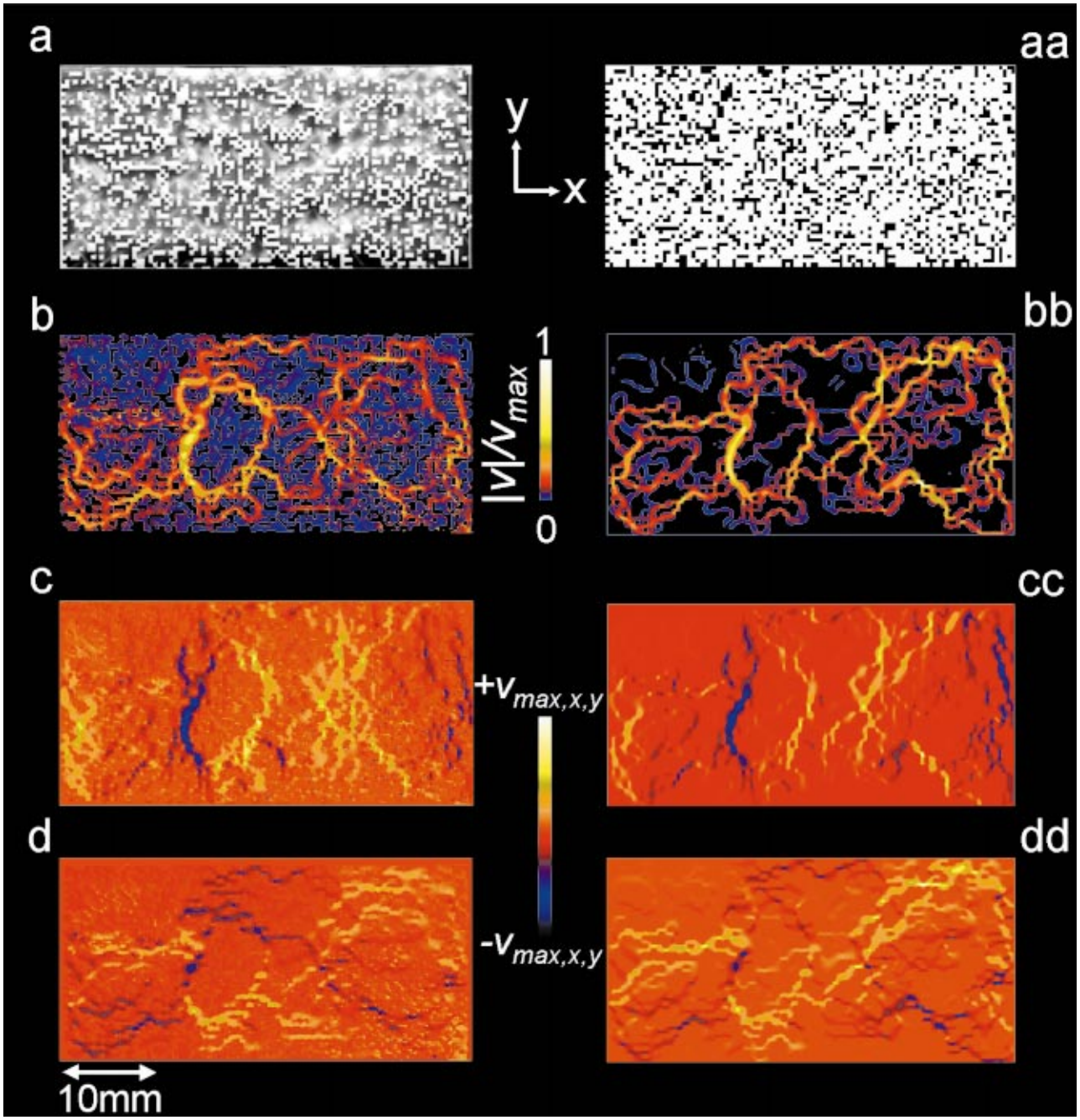

FIG. 4. (Color) Comparison between experimental (left) and computed (right) maps of a random-site percolation cluster with a porosity of $p=0.7$ in a Rayleigh-Bénard configuration. The NMR experiments and the simulations refer to silicon oil. (a) Photograph of the model object. (aa) Computer generated template. (b) NMR map of the velocity magnitude of the convective flow patterns. (bb) Simulated map of the velocity magnitude. (c) NMR map of the y component of the velocity (vertical). (cc) Simulated map of the y component. (d) NMR map of the x component of the velocity (horizontal). (dd) Simulated map of the x component. The standard deviation of all experimental velocity maps was $\sigma \leqslant 10^{-2}$ mm/s.

too weak to permit the desired temperature resolution, a different fluid was chosen for this purpose. Ethylene glycol turned out to be particularly favorable. Figure 5 shows a calibration curve recorded in the range 293 to 353 K. This suggests the empirical relation

$$T(T_1) = 36.7 \ln\left(\frac{T_1}{0.18 \text{ ms}}\right) \text{K} \pm 2 \text{ K}, \qquad (2)$$

where T_1 refers to a Larmor frequency of 200 MHz.

In the temperature mapping experiments, the repetition time was varied from 0.2 s to 6.4 s with an increment of 0.2 s. Figure 6 shows the results of a test experiment demonstrating the stationary temperature distribution in a cell with a temperature gradient in this case directed from the bottom to the top of the cell. The temperature gradients in vertical and horizontal directions are constant as expected for a bulk

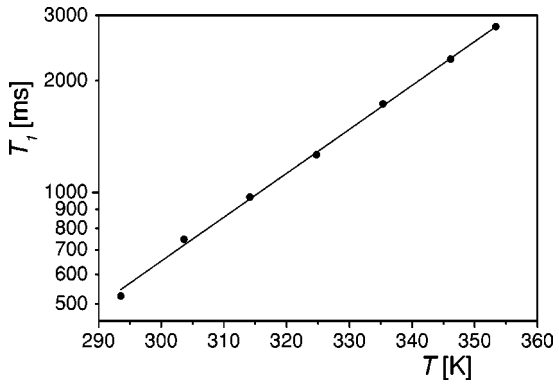

FIG. 5. Calibration curve of the proton spin-lattice relaxation time of ethylene glycol at 200 MHz as a function of the temperature. The solid line represents $T_1 = 0.18 \exp\{T/36.7\ \mathrm{K}\}$ ms.

sample with a homogeneous thermal conductivity distribution.

IV. COMPUTATIONAL FLUID DYNAMICS METHODS

Parallel to all experimental investigations numerical simulations have been performed with the aid of the finite-volume method (FVM; commercial software package FLUENT 5.5) [22,23] for the same percolation networks.

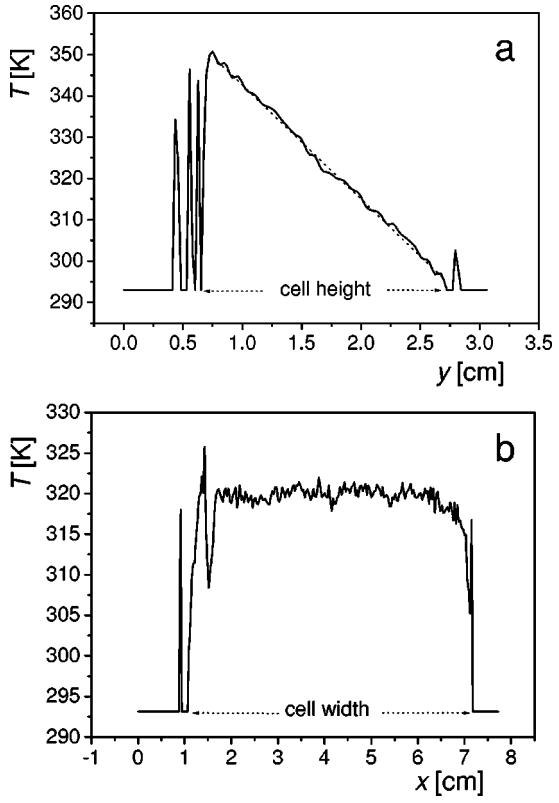

FIG. 6. Experimental temperature test profiles measured across the cell middle in the vertical (a) and horizontal (b) directions. The cell was filled with bulk ethylene glycol. An upward temperature gradient was applied so that no convection took place. The dotted line in (a) represents a constant temperature gradient along the y direction. The temperature profile in the horizontal direction is constant with the exception of the edges where the imperfect insulation caused some deviations.

The FVM simulations are based on the Boussinesq approximation [4], that is, all hydrodynamic parameters are kept fixed with the exception of the temperature dependent density. These assumptions are certainly justified in the temperature range of our experiments. The program numerically solves the Navier-Stokes, the continuity, and the heat-conduction equations with geometrical boundary conditions given by the matrix and the convection cell. Molecular diffusion was not taken into account in the simulations. However, the good coincidence of the simulated and the experimental data suggests that no major influence of Brownian motion matters here at least in the range that can be probed with NMR velocity mapping ($v \geqslant 0.01$ mm/s).

The boundary conditions at the side walls of the convection cell were assumed to be adiabatic, whereas the top and bottom surfaces are subject to isothermic conditions. Within the porous medium the solid polystyrene and the fluid in the pore space are thermodynamically coupled according to the respective heat conductivities. The fluid is assumed to comply to nonslip conditions at the pore walls so that the velocity vanishes at all surfaces.

Each point of the 100×50 square lattice on which the percolation clusters are based was meshed by 7×7 elements. The results deviate from a 5×5 mesh coverage by 20% and from a 40×40 mesh coverage by $<5\%$. The total number of 700×350 equidistant elements turned out to be sufficient for the spatial resolution to be considered in the light of the fabrication and measuring limits in the order of several hundred micrometers. Note, however, that the resolution of the discreteness restricts the size of the smallest vortices that are taken into account in the computational fluid dynamics simulation. The only criterion that permits the justification of a certain finite resolution is the comparison with a real experiment. This will be shown in the following section.

The global residue of the simulations was $<10^{-5}$. The temperature and velocity convergence of the numerical approach was additionally surveyed in selected lattice cells. Before solving the Navier-Stokes equation for the flow velocity, the program was initialized by first calculating the temperature field for the static case.

The finite thickness of the model objects perpendicular to the flow plane was not taken into account in the simulations. That is, the absence of friction at the bounding surfaces of the quasi-two-dimensional objects leads to flow velocities in the simulations increased by a factor of about 4 relative to the NMR velocity mapping experiments. The experimental result may also appear to be slightly decreased by partially filled voxels at the matrix edges, whereas the simulations are referring to completely filled voxels perfectly fitting to the matrix structure.

The fluid parameters assumed in the computational fluid dynamics simulations correspond to the fluids used in the experiments. Also the thermal conductivity of the polystyrene matrix deviating from that of the fluids was accounted for. Apart from the deviating velocity values explained above, the quality of the computational fluid dynamics simu-

lations is demonstrated by the coinciding flow patterns shown in Fig. 4.

V. RESULTS FOR RANDOM-SITE PERCOLATION CLUSTERS

A. Temperature maps

In an ideal Rayleigh-Bénard cell filled with a free fluid thermal convection, that is coherent flow, remains absent until a critical value of the Rayleigh number is reached. Ordinary heat conduction dominates until then. The Rayleigh number, in particular, depends on the temperature difference between the bottom and top compartment surfaces. Under such circumstances the temperature gradient is directed in vertical direction from the bottom to the top. No horizontal components exist below the critical Rayleigh number [compare Fig. 6(b)].

A similar situation arises in porous media only if the thermal conductivity of the matrix happens to be identical to that of the fluid. The temperature gradient remains directed vertically below a critical Rayleigh number that exists as in the bulk liquid. In this case we are again facing a crossover from heat transport solely by conduction to thermal convection dominating above the critical temperature difference.

However, heat conductivities of solid matrix materials and of fluids normally are different. That is, the temperature distribution can no longer be described by vertical-temperature gradients alone even at the lowest temperature differences between the bottom and top surfaces of the cell. Finite horizontal-temperature gradient components arise, and, as a consequence, coherent convection rolls exist under any circumstance as far as the connectivity of the pore space allows. Figure 7(a) shows a temperature map in a random-site percolation network for a completely insulating matrix material, Fig. 7(b) the corresponding horizontal-temperature profile in the middle of a network with the respective heat conductivities of solid polystyrene and silicon oil.

Figure 8 shows temperature maps measured (a) and simulated (aa) in a random-site percolation cluster with a porosity $p=0.7$ in a Rayleigh-Bénard configuration. The good coincidence of the experimental and calculated maps demonstrates the quality both of the measuring and the simulation technique.

The temperature varies in horizontal as well as in vertical direction. However, the strongest temperature gradients show up in downward direction. The vertical velocity component are correspondingly strong and lead to marked main flow paths more or less aligned along the temperature gradient direction as visualized in the maps of the velocity components shown in Figs. 8(b), (bb), (c), and (cc).

B. Histograms of the flow velocity

The experimental and simulated velocity maps like those shown in Figs. 4 (silicon oil) and 8 (ethylene glycol) were evaluated with respect to distributions of the velocity components and of the velocity magnitude (in units of the respective maximum velocity component or magnitude). For the evaluation of the histograms, the velocity component or

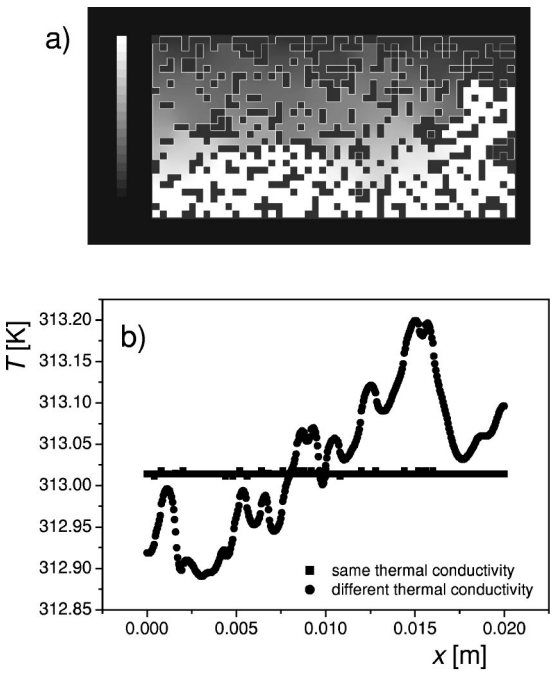

FIG. 7. Calculated temperature distribution in a random-site percolation network in the absence of coherent flow and under the assumption of different thermal conductivities in the fluid and in the matrix. Under such conditions horizontal-temperature gradients arise. (a) Temperature map calculated for a completely insulating solid matrix (thermal conductivity 0; $p=0.6375$). (b) Temperature profile along a horizontal line in the middle of a network with $p=0.5$. The thermal conductivities of solid polystyrene and silicon oil KT5 were assumed in this case. The straight line was evaluated assuming equal thermal conductivities in the matrix and in the fluid for comparison.

magnitude was determined at each knot in the meshed area. The total velocity range, $0 \leqslant v \leqslant v_{max}$, was subdivided into up to 10 000 equal bins. The abundance of the corresponding knot velocities was then counted and plotted in normalized, logarithmic form.

Figure 9 shows histograms of the relative velocity magnitude evaluated from simulated velocity maps for different porosities at a fixed overall temperature difference $\Delta T=40$ K between the bottom and the top cover. The potential extensions of the convection loops depends on the pore space restrictions (compare Figs. 4 and 8). The lower the porosity is the smaller can the convection loops develop. Given an overall mean temperature gradient, the local temperature difference across a convection loop is a function of the loop size, and, hence, of the porosity. The consequence is that the maximum velocity decreases with decreasing porosity. This must be kept in mind when considering histograms of relative velocities for fixed overall temperature differences.

The histograms in Fig. 9 are generally characterized by a flat section at low relative velocities and a sharp drop near the maximum velocities. The low- and high-velocity regions of the histograms can be attributed to localized and cluster-spanning convection rolls, respectively. Between $p=0.635$ and $p=0.65$ the distribution changes significantly for low relative velocities. As will be outlined in the following sec-

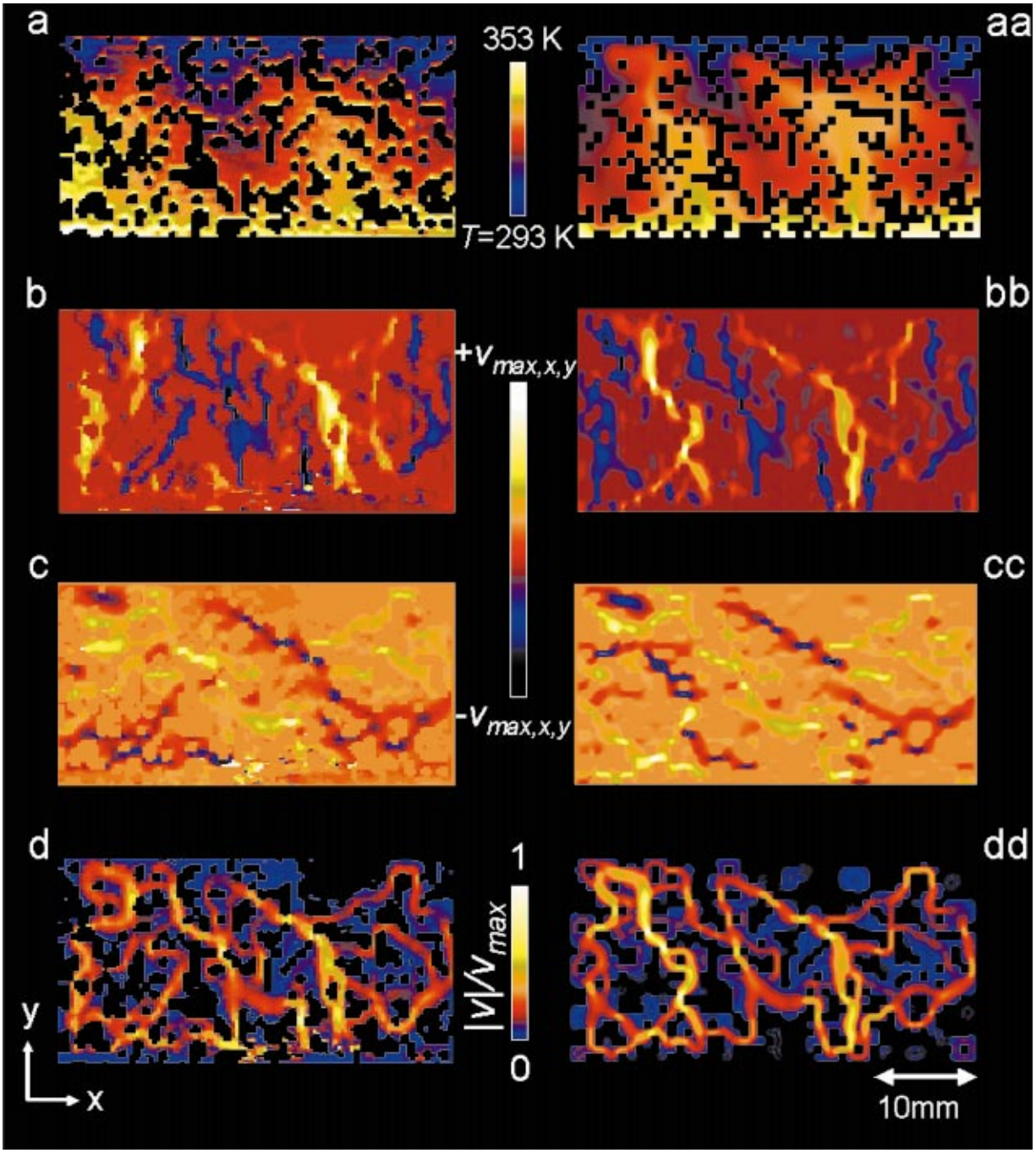

FIG. 8. (Color) Comparison of temperature and velocity maps for ethylene glycol in random-site percolation clusters with a porosity of $p=0.7$ in a Rayleigh-Bénard configuration. Left column: NMR experiments. Right column: simulations. (a) and (aa) temperature maps. (b) and (bb) maps of the velocity y component. (c) and (cc) maps of the velocity x component. (d) and (dd) maps of the velocity magnitude.

tion, this can be attributed to a critical phenomenon attributed to features both of the known Rayleigh-Bénard instability and the geometrical percolation threshold [5].

At low velocities, $v<v_{max}/100$, and for $0.6\leqslant p<0.75$ (v) and $0.6\leqslant p<0.9$ ($v_{x,y}$) the data appear to approach a power law

$$n\propto v^{-b}, \tag{3}$$

a tendency that is further corroborated by histograms of the magnitude and the two components of the velocity evaluated at different porosities for a fixed maximum velocity (Fig. 10).

To keep the maximum velocity fixed independent of the porosity means that the local temperature difference across a convection loop tends to be the larger the smaller the loop is, that is the smaller the porosity is. This rescales the velocity distribution which now refers to the absolute velocities rather than relative values. The power law given in Eq. (3) again describes the histograms at low velocities in a wide range in

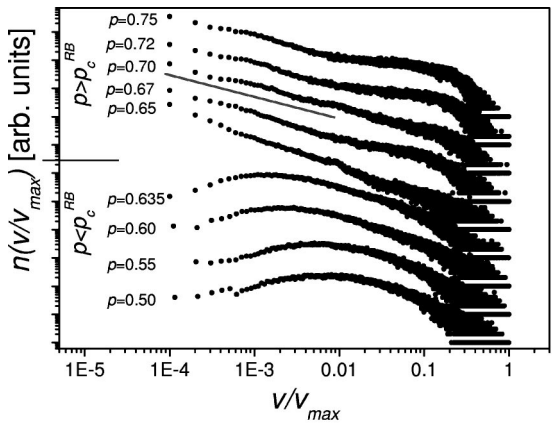

FIG. 9. Double logarithmic velocity histograms evaluated from FVM simulated free-convection patterns in two-dimensional random-site percolation networks in a 2-cm-high Rayleigh-Bénard configuration. The data for different porosities p are plotted shifted relative to each other versus the ratio of the magnitudes of the local velocity and the maximum value, v/v_{max}. The y axis represents the vertical direction. The data refer to a fixed overall temperature difference of $\Delta T=40$ K and the material-specific parameters of silicon oil in a polystyrene matrix. The velocity scale was linearly subdivided in 10 000 intervals. Note that the data point symbols overlap at high velocities owing to the logarithmic scale. The scattering of the data is due to the much lower abundance in this range. The straight line corresponds to a power law.

the Rayleigh-Bénard-convection regime. (Note that the critical phenomenon describing the onset of Rayleigh-Bénard convection sensitively depends on the mean temperature gradient, and, hence, will be shifted with the overall temperature difference to different critical p values. See the discussion in the following section.)

The exponent b evaluated from these data for $v<v_{max}/100$ is plotted in Fig. 11 as a function of the porosity. It appears that it obeys a linear relationship

$$b=c_1p+c_2, \tag{4}$$

for $0.6\leqslant p\leqslant 0.9$ where c_1 and c_2 are constants. Interestingly the results of the present convection study show some features similar to those found in flow studies [24,25].

The data in Figs. 9 and 10 at large velocity magnitudes and close to $p=0.65$ can be described by an exponential law

$$n\propto\exp\{-c_3v/v_{max}\} \tag{5}$$

in a range $0.1\leqslant v/v_{max}\leqslant 1$ in excellent agreement with the data evaluated from the experimental velocity maps. The quantity c_3 is a constant. The (horizontal) x component appears to follow also an exponential decay of the histogram [Fig. 12(b)] whereas the (vertical) y component significantly deviates from any such law [Fig. 12(c)].

C. The Rayleigh-Bénard-percolation transition

The classical Rayleigh-Bénard transition occurs in bulk fluids in a horizontally infinitely wide convection cell at a certain critical value of the Rayleigh number [4]

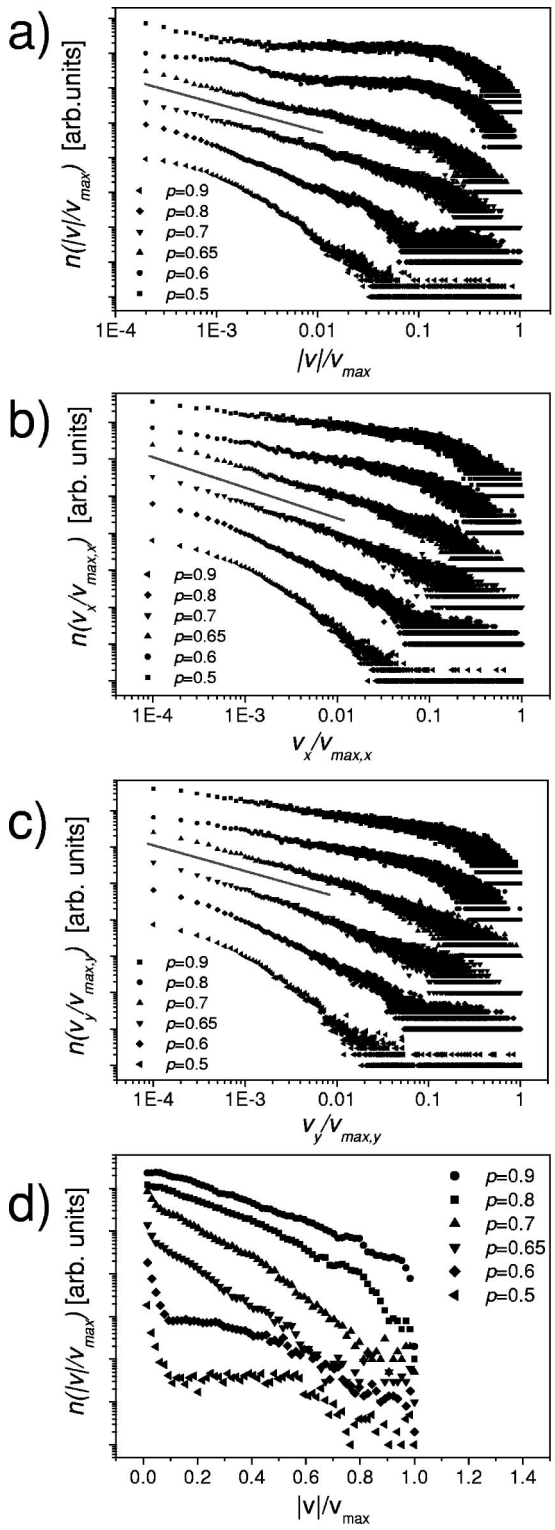

FIG. 10. Velocity histograms for the same system as in Fig. 9 but now for a fixed maximum velocity of $v_{max}\approx 0.3$ mm/s instead of a fixed overall temperature difference ΔT which is varied correspondingly. (a) Magnitude, bin size $v_{max}/10\,000$; (b) (positive) x component, bin size $v_{max,x}/10\,000$; (c) (positive) y component, bin size $v_{max,y}/10\,000$; (d) magnitude, bin size $v_{max}/64$ (half logarithmic representation). The straight lines in plots (a) to (c) correspond to power laws.

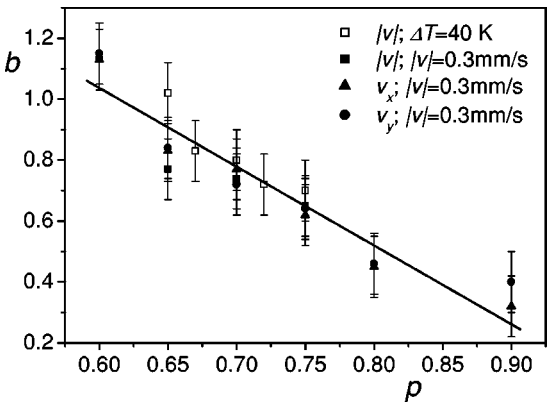

FIG. 11. Exponent b evaluated from the histograms shown in Figs. 9 and 10 according to the respective power laws $n \propto |v|^{-b}$, $n \propto v_x^{-b}$, and $n \propto v_y^{-b}$ as functions of the porosity p. The straight line corresponds to a linearly decaying law $b = c_1 p + c_2$.

$$R_a = \frac{g \alpha \rho c_p \Delta T d^3}{\nu \lambda}, \tag{6}$$

where g is the gravitational acceleration, and ΔT and d are the temperature difference and the distance between the bottom and top, i.e., the heating and cold baths, respectively. The other parameters are specific for the fluid: α is the thermal expansion coefficient, ρ_0 is the density at the temperature of the cold bath, c_p is the specific heat at constant pressure, ν is the kinematic viscosity, and λ is the thermal conductivity.

The critical value of the Rayleigh number is 1708. Below this value we have pure thermal conduction. The onset of thermal convection occurs when the critical value is reached. For a given fluid and a given convection cell the Rayleigh number can be varied by varying the overall temperature difference ΔT. In view of the present study, convective flow is monitored via the maximum velocity occurring in any of the fluid voxels in the cell. Figure 13 shows a corresponding simulation result. The maximum velocity magnitude jumps at the critical Rayleigh number up by at least 11 orders of magnitude, where the lower value is determined by the finite simulation precision (''double precision''). The critical Rayleigh number is found to be somewhat larger than the value given above due to the finite lateral extension of the cell configuration assumed [3].

The convection loops developing in the pore space of a random-site percolation cluster are getting more and more distorted with decreasing porosity. This is visualized in the series of simulated flow patterns shown in Fig. 14. Cell-spanning convection loops are only possible significantly above the geometrical percolation threshold where such closed pathways are more likely. The geometrical percolation threshold is by contrast defined by a single cluster spanning pathway rather than by a closed loop.

When the percolation threshold is approached and the porosity falls short of it, the convection loops are getting more and more localized. Below the percolation threshold the maximum loop extension is restricted by the correlation length of the network which determines the mean size of the clusters [1]. At extremely low porosity values loops are even restricted to microscopic portions of a pore channel and do not hem about matrix obstacles anymore.

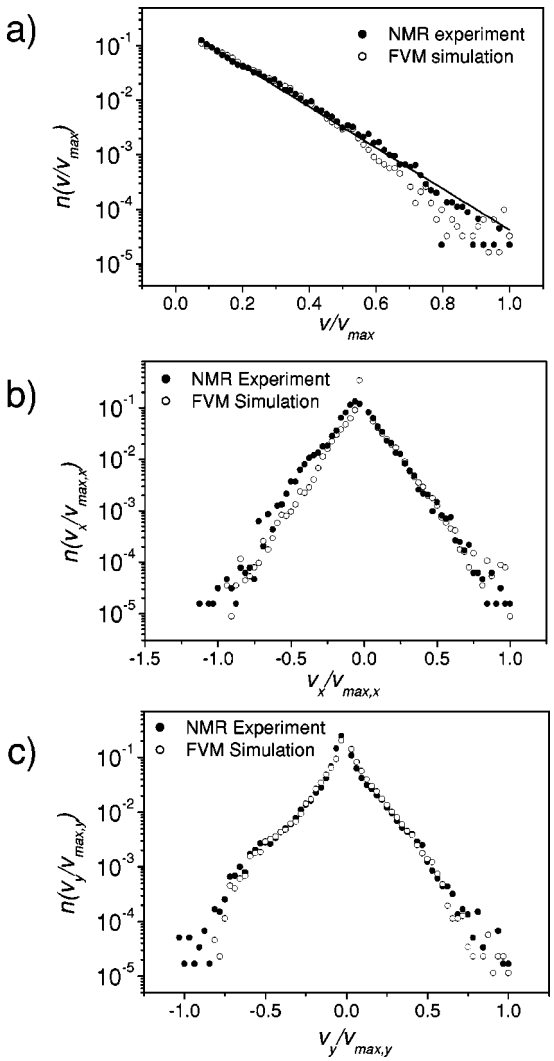

FIG. 12. Comparison of experimental and simulated velocity histograms in the experimentally accessible range $v > 0.01$ mm/s. (a) Magnitude; (b) x component; (c) y component. The bin sizes were 1/64 and 1/32 of the maximum velocity and velocity components, respectively.

The more or less restricted extension of the convection loops occurring in the pore space simultaneously reduces the temperature difference effective for the loops. Cluster spanning loops certainly are subject to the overall temperature difference in the cell, whereas more localized loops sense only a fraction given by the temperature gradient and the loop extension. Any critical onset of thermal convection in a percolation network will thus depend on the porosity and the overall temperature dependence.

The transition phenomenon showing up in the histograms in Fig. 9 at a certain critical porosity can be examined in more detail by plotting the maximum velocity as a function of the porosity p where the overall temperature difference ΔT in the convection cell is an experimental parameter.

The maximum velocities change dramatically with the po-

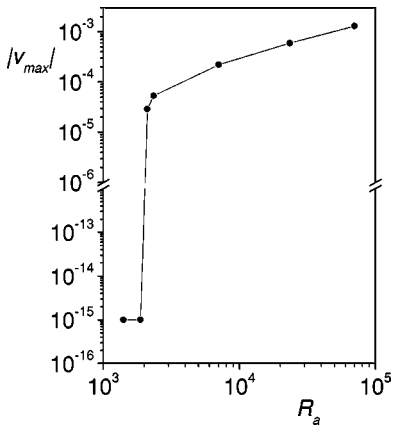

FIG. 13. Ordinary Rayleigh-Bénard transition in a convection cell filled with a bulk fluid. The instability reveals itself by an abrupt increase of the maximum velocity when the critical Rayleigh number is reached. The two lower data points correspond to the numerical accuracy achievable in our simulations.

rosity at certain critical values depending on the overall temperature difference. Figure 15 shows a corresponding plot. For $\Delta T = 40$ K an abrupt change of at least two orders of magnitude of the maximum velocity occurs at a certain critical porosity. The value of the critical porosity is a function of the system size to a minor degree [5], and in a more pronounced way of the overall temperature difference ΔT.

The latter finding corroborates that this transition phenomenon is of a truly critical nature and that it combines features of both the geometrical percolation transition and the Rayleigh-Bénard instability: The transition phenomenon observed here occurs when in the geometrically largest possible closed-loop pathway the Rayleigh-Bénard instability conditions are fulfilled. The loops that are possible at minor porosities tend to be small. The transition to the Rayleigh-Bénard convection regime hence requires a large overall temperature difference in order to ensure a sufficient temperature gradient in the loop range. Vice versa, large porosities permit large loops, and the Rayleigh-Bénard instability conditions are already given at a moderate overall temperature difference.

The finite step height at the critical porosities observed in Fig. 15 is a consequence of the horizontal-temperature gradients occurring even in the absence of convection if the thermal conductivities in the fluid and in the matrix are deviating (see the temperature maps shown in Figs. 7 and 8). The consequence is that some moderate convective flow already exists below the critical porosities: There is no critical threshold for the onset of convective flow in horizontal-temperature gradients [3].

On the other hand, horizontal-temperature gradients can be avoided in the simulations by choosing identical thermal conductivities in the fluid and in the matrix. In this case no flow can be monitored below the critical porosities at the respective overall temperature difference, and the velocity drops below the finite simulation accuracy value. Some data points demonstrating this are also plotted in Fig. 15.

Figure 15 suggests that the transition to the Rayleigh-Bénard convection regime reveals itself when the maximum velocity takes the value $v_{max} \approx 0.3$ mm/s under the conditions of the convection cell subject to our simulations. The relationship between the critical porosity and the corresponding overall temperature difference, $p^{RB} = p^{RB}(\Delta T^{RB})$, or vice versa $\Delta T^{RB} = \Delta T^{RB}(p^{RB})$ can thus be established from the set of velocity maps simulated for different porosities and overall temperature differences: Selecting those combinations that fulfill the condition $v_{max} \approx 0.3$ mm/s $\pm 20\%$ yields the data shown in Fig. 16.

The semilogarithmic plot of the data $\Delta T^{RB} = \Delta T^{RB}(p^{RB})$ suggest three regimes: Two exponential functions at low and high p^{RB} values separated by a crossover interval at a particular value $p_c^{RB} \approx 0.6$ corresponding to the overall temperature difference of our system ΔT_c^{RB}. In the exponential regions the critical porosity can be represented by the laws

$$\Delta T^{RB} = T_0 \exp\{-p^{RB}/u\}, \tag{7}$$

or vice versa,

$$p^{RB} = \ln\left\{\left(\frac{T_0}{\Delta T^{RB}}\right)^u\right\}, \tag{8}$$

where T_0 is a constant and $u = 0.105 \pm 0.005$.

The crossover at the experimental parameter combination $p = p_c^{RB}$ and $\Delta T = \Delta T_c^{RB}$ occurs when sample-spanning convection loops become possible for the first time coming from low porosities (and low temperature differences) as visualized in the series of flow patterns shown in Fig. 14. That is, at this particular porosity and at this particular temperature difference the geometrical percolation threshold (modified for closed loops and finite systems) and the Rayleigh-Bénard transition (modified for porous media) coincide. Both critical phenomena are superimposed at this particular value pair. It must therefore be considered as a distinguished porosity and temperature difference combination. We call it the ''Rayleigh-Bénard-percolation transition'' [5].

On the other hand, the instabilities occurring at $p^{RB}, \Delta T^{RB}$ parameter pairs below or above the Rayleigh-Bénard-percolation threshold $p_c^{RB}, \Delta T_c^{RB}$ (see Fig. 15) reflect ordinary Rayleigh-Bénard transitions modified for porous media. The instabilities occurring at porosities above p_c^{RB} are connected with the appearance of sample-spanning convection loops of little restraint by the percolation network. At lower porosities, no sample-spanning loops are possible any longer. The convection rolls adopt a more localized character, and the local cluster diameter determines the effective temperature difference.

VI. DISCUSSION

Thermal convection in random-site percolation clusters in a Rayleigh-Bénard configuration was studied using magnetic resonance velocity and temperature mapping in comparison to computational fluid dynamics simulations. Plotting the maximum velocity detected in a voxel as a function of experimental parameters (porosity, overall temperature difference) turned out to be a dependable way of detection.

The computational fluid dynamics calculations provide

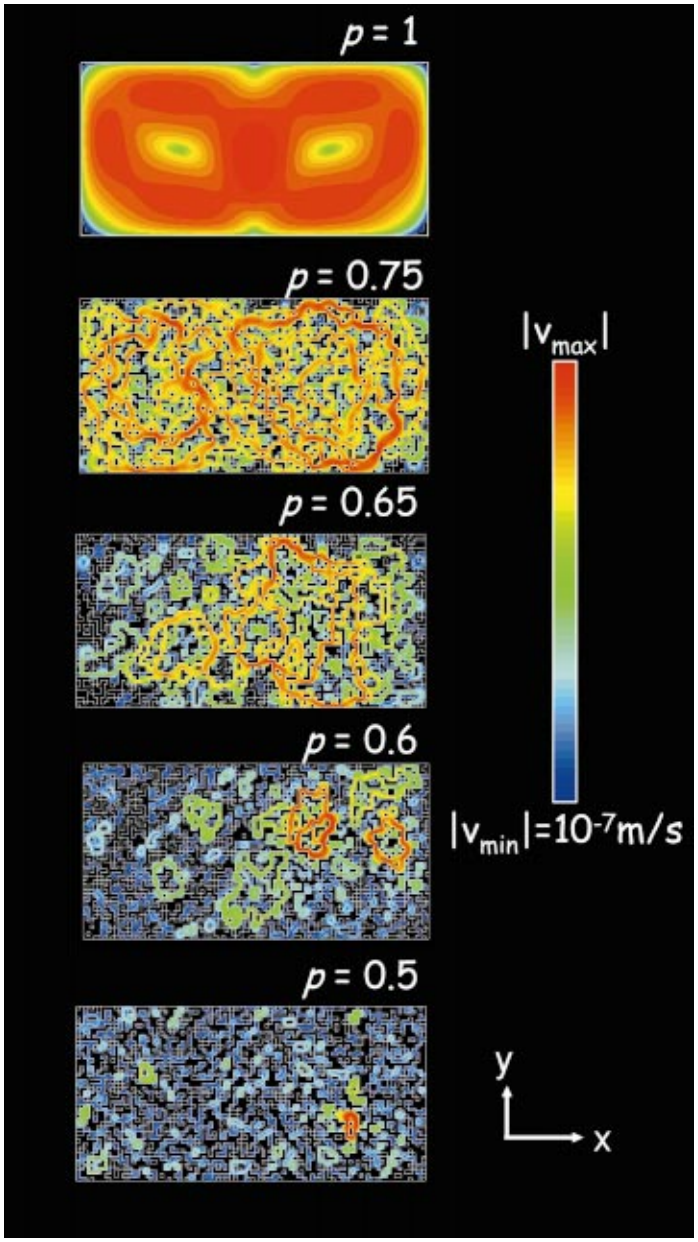

FIG. 14. (Color) Logarithmic contour plots of the velocity magnitude for different porosities and a fixed maximum velocity of $v_{max} \approx 0.3$ mm/s.

numerical solutions of the Navier-Stokes equation, the continuity equation, and the heat-conduction equation. In the light of the relatively good coincidence of the simulated and experimental flow patterns, we conclude that FVM simulations provide a reasonably reliable tool for examining velocity distributions in the submillimeter-per-second range.

The advantage of FVM simulations is that the accessible velocity range is much broader than in the NMR velocity mapping experiments which are limited by a finite-velocity resolution (in the present case 0.01 mm/s). NMR velocity mapping is therefore not feasible below the Rayleigh-Bénard transitions where flow velocities are getting extremely small even in the presence of pretransitional convection. On the other hand, the abrupt occurrence of detectable flow velocities when passing the Rayleigh-Bénard transitions (modified for porous media) in general and at the Rayleigh-Bénard-percolation threshold, in particular, is an experimental verification of the existence of these phenomena.

The velocity maps recorded in this study visualize the changes of the convection loops when the geometric flow restrictions are changed. With decreasing porosity, sample-spanning rolls become less and less likely until a modified percolation transition occurs. At a certain value of the porosity $p = p_c^{RB}$ combined with a certain overall temperature difference $\Delta T = \Delta T_c^{RB}$ the Rayleigh-Bénard-percolation instability occurs as a phenomenon of a mixed geometrical and hydrodynamic nature. The transition parameters are specific for the type and size of the percolation network under investigation.

Below and above the Rayleigh-Bénard-percolation instability, where the ordinary Rayleigh-Bénard transition (modified for porous media) and the geometrical percolation threshold do not coincide, critical transition phenomena nevertheless occur as demonstrated in Fig. 15, if the overall temperature difference allows for a Rayleigh-Bénard transi-

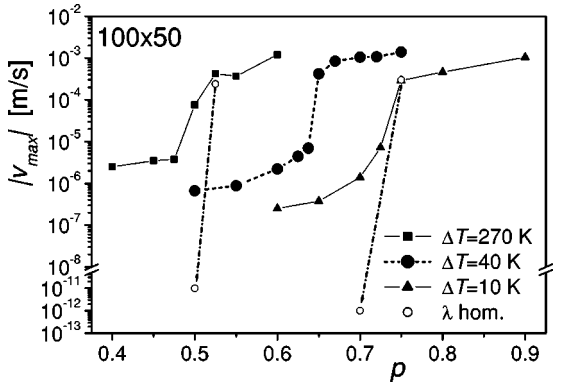

FIG. 15. Maximum convective flow velocity as a function of the porosity of a random-site percolation network. The abrupt changes of the maximum velocity indicate transitions (modified for porous media) with the overall temperature difference ΔT as a parameter. The data for $\Delta T = 40$ K are close to the Rayleigh-Bénard-percolation instability at $p \approx 0.6$, where the hydrodynamic Rayleigh-Bénard phenomenon and the geometrical percolation threshold (modified for closed loops) of the percolation network coincide (see Fig. 16). The finite flow velocities found below the thresholds are due to pretransitional convection arising from horizontal-temperature gradients. This superimposed convection disappears when the thermal conductivities λ in the fluid and in the matrix are assumed to be identical as demonstrated by the data represented by open circles and arrows. The lower values of the open-circle data points correspond to the numerical resolution adjusted; that is, no finite velocity can be stated below the transitions under these conditions.

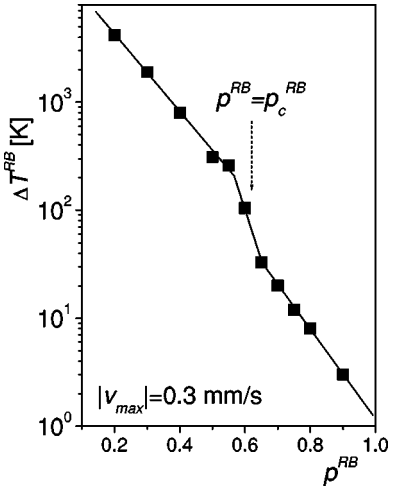

FIG. 16. Relationship between the overall temperature difference and the Rayleigh-Bénard transition defined by the occurrence of a maximum velocity value of $v_{max} = 0.3$ mm/s. The crossover at the Rayleigh-Bénard-percolation threshold at $p = p_c^{RB} \approx 0.6$ and $\Delta T = \Delta T_c^{RB} \approx 110$ K indicates the coincidence of the Rayleigh-Bénard instability (modified for porous media) and the geometrical percolation transition (modified for closed-loop flow pathways).

tion of the ordinary type but modified for topological constraints of porous media.

The distinguished character of the Rayleigh-Bénard-percolation instability as a combination of two critical phenomena is demonstrated in Fig. 16, where the critical overall temperature difference of the convection cell and the critical porosity are correlated. The Rayleigh-Bénard percolation reveals itself as a crossover between two regimes characterized by shifted exponential relations representing the ordinary combined Rayleigh-Bénard-percolation instability transition below and above the combined Rayleigh-Bénard-percolation instability. That is, there is no variation degree of freedom for the combined Rayleigh-Bénard-percolation instability: The threshold conditions for both critical phenomena must be fulfilled at one time, whereas the ordinary Rayleigh-Bénard transition can occur at any finite porosity at the effective temperature difference corresponding to the convection roll size geometrically possible.

The data points plotted in Fig. 16 refer to random-site percolation networks and to the particular system size and material parameters relevant in our study. Increasing the system thickness d (which, however, would conflict with our present experimental and computational restrictions) is expected to heighten the crossover step. At porosities above p_c^{RB}, the critical overall temperature difference would be reduced [see Eq. (6)], whereas it would be increased below p_c^{RB} so that the local loop-spanning temperature gradient retains its critical value. Vice versa, decreasing d is expected to flatten the crossover step.

The temperature maps shown in Fig. 8 visualize that horizontal gradients arise even in the absence of hydrodynamic flow if the thermal conductivities of the fluid, and the matrix deviate from each other. The consequence is that (very slow) convective flow occurs already below the Rayleigh-Bénard thresholds. However, this pretransitional flow is not of a critical nature. If the thermal conductivities of the fluid and the matrix happen to coincide, no such pretransitional convection occurs as demonstrated by our computational fluid dynamics simulations (see Fig. 15).

In order to characterize convective transport in terms of the velocity statistics, we have evaluated histograms of the velocity maps as a function of the porosity. The histograms are characterized by a steep high-velocity cut-off attributed to the cluster-spanning convection rolls and a slowly varying region characteristic for more localized convection connected with velocities $v < v_{max}/100$. Above the Rayleigh-Bénard transition the latter regime can be represented by a power law with an exponent depending on the porosity. On the other hand, the velocity distribution of the cluster-spanning loops appears to follow an exponential law in the vicinity of p_c^{RB}.

ACKNOWLEDGMENTS

We thank Andreas Klemm and Hans Wiringer for their kind cooperation. This work was supported by the Deutsche Forschungsgemeinschaft (Grant No. SFB569).

[1] D. Stauffer and A. Aharony, *Introduction to Percolation Theory* (Taylor and Francis, London, 1992).
[2] D. A. Nield and A. Bejan, *Convection in Porous Media* (Springer-Verlag, Berlin, 1992).
[3] G. P. Merker, *Konvektive Wärmeübertragung* (Springer-Verlag, Berlin, 1987).
[4] D. J. Tritton, *Physical Fluid Dynamics* (Oxford Science Publication, Oxford, 1988).
[5] M. Weber, A. Klemm, and R. Kimmich, Phys. Rev. Lett. **86**, 4302 (2001).
[6] N. Jan, Physica A **266**, 72 (1999).
[7] H.-P. Müller, J. Weis, and R. Kimmich, Phys. Rev. E **52**, 5195 (1995).
[8] A. Klemm, H.-P. Müller, and R. Kimmich, Phys. Rev. E **55**, 4413 (1997).
[9] R. Kimmich, *NMR Tomography, Diffusometry, Relaxometry* (Springer-Verlag, Berlin, 1997).
[10] S.J. Gibbs, T.A. Carpenter, and L.D. Hall, J. Magn. Reson. **105**, 209 (1993).
[11] J. Weis, R. Kimmich, and H.-P. Müller, Magn. Reson. Imaging **14**, 319 (1996).
[12] M.D. Shattuck, R.P. Behringer, G.A. Johnson, and J.G. Georgiadis, Phys. Rev. Lett. **75**, 1934 (1995).
[13] L. Howle, R.P. Behringer, and J. Georgiadis, Nature (London) **362**, 230 (1993).
[14] T.W. Redpath, D.G. Norris, R.A. Jones, and R.M.S. Hutchinson, Phys. Med. Biol. **29**, 891 (1984).
[15] G. Bodenhausen, R. Freeman, and D.L. Tuner, J. Magn. Reson. **27**, 511 (1977).
[16] Michael Heidenreich, Ph.D. thesis, Universität Ulm, 1999 (unpublished).
[17] R. Kimmich, K. Bühler, and A. Knüttel, J. Magn. Reson. (1969-1992) **93**, 256 (1991).
[18] N. Hedin and I. Furo, J. Magn. Reson. **131**, 126 (1998).
[19] C.S. Zuo, K. Metz, Y. Sun, and A.D. Sherry, J. Magn. Reson. **133**, 53 (1998).
[20] N.M. Loening and J. Keeler, J. Magn. Reson. **139**, 334 (1999).
[21] A. Jerschow, Geomagn. Aeron. **145**, 125 (2000).
[22] J. D. Anderson, *Computational Fluid Dynamics* (McGraw-Hill, New York, 1995).
[23] C. Cuvelier, A. Segal, and A. van Steenhoven, *Finite Element Methods and Navier-Stokes Equations* (Reidel, Dordrecht, 1988).
[24] J.S. Andrade, Jr., M.P. Almeida, J. Mendes Filho, S. Havlin, B. Suki, and H.E. Stanley, Phys. Rev. Lett. **79**, 3901 (1997).
[25] H.A. Makse, J.S. Andrade, Jr., and H.E. Stanley, Phys. Rev. E **61**, 583 (2000).